# Chapter-7

# Fluorescent CNDs from Quercetin and their various applications

## 7.1 Introduction

Carbon nanodots (CNDs) as a nano-probes are integrated systems over 100 times smaller than cells, with sizes on par with or lower than pores and apertures in the human body's vasculature and tissues. They integrate fundamental concepts from chemical biology, pharmaceutical engineering, and other fields to investigate and design nanomaterials [Marin *et al.,* 2022, Koo *et al.,* 2011]. Since CNDs can easily incorporate valuable compounds such as active targeting moieties, imaging agents, or medicines through conjugation or simple loading, they offer wide applications across biomedical and environmental domains [Huang *et al.,* 2018] Smart design and innovative development can impart multi-functional attributes to nano-probes. Several CNDs can be degraded or disassembled under certain stimuli such as pH and temperature to release their contained molecules. At the same time, some are based on fluorescence quenching phenomena that are activated under certain conditions [Zhang *et al.,* 2016, Chi *et al.,* 2012].

For bio-sensing applications, CNDs can be used as fluorescent nano-probes. They can be easily fabricated using various cost-effective and environment-friendly methods, and biomolecules can be used to achieve the requisite biosensing properties [Su *et al.,* 2022]. CNDs have been reported to possess applications in bioimaging, drug delivery, metal

sensing, antibacterial agents, etc. Flavonoids are ubiquitous polyphenolic chemicals that are characterized by the flavan nucleus and are found in a wide range of fruits, vegetables, and plant-derived beverages. Quercetin is a polyphenolic compound bearing a flavone moiety with two benzene rings linked by a heterocyclic pyrrole ring and diphenyl propane basic skeleton. Quercetin exhibits anticancer, anti-inflammatory, and antioxidant potential in various studies reported in cellular and animal models via regulating the gene expression and signaling pathways [Patra *et al.,* 2018]

PEGylation of protein/peptide therapeutics and conventional nanoparticles is frequently employed since it is a non-immunogenic and highly water-soluble polymer [Hoffmann *et al.,* 2022]. Polyethylene glycol has recently been actively researched for its unique capacity to enhance CNDs' fluorescence emission, revealing CNDs generation and photoluminescence mechanism. Andrographolide is the major phytomolecule present in *Andrographis paniculata* (AP), belonging to the family of Acanthaceae, which has been projected as a potential medicinal moiety in various traditional medicinal systems. Various biological activities such as anti-cancer, anti-inflammatory, anti-oxidant have been reported for this labdane diterpenoid lactone [Tian *et al.,* 2022].

To the best of our knowledge, this is the first original report demonstrating the utility of Quercetin-based CNDs for $As^{3+}$ and $Fe^{3+}$sensing, drug delivery, anticancer therapy, antimicrobial therapy, and free radical scavenging potential.

## 7.2 Experimental section

### 7.2.1 Materials and chemicals

All procured solvents and reagents were used directly as purchased. Quercetin and Sulforhodamine B were procured from Sigma-Aldrich. DPPH (1, 1-diphenyl-2-picrylhydrazyl), methanol, dichloromethane, etc., were purchased from Merck. Deionized water (conductivity:18.2 MH $cm^{-1}$) was obtained using a Millipore water purification system.

### 7.2.2 Fabrication of quercetin-based CNDs

A simple, one-step hydrothermal synthesis approach was employed to fabricate quercetin-based CNDs. 200 mg of quercetin was mixed with 45 mL water and 5 mL ethanol in a solution. At 50°C, the mixture was vigorously agitated for 30 minutes. The resulting solution was then subjected to an 8 h hydrothermal treatment at 160°C. After cooling the system, the dark brown solution was subjected to centrifugation at 11,000 rpm for 15 minutes to separate the insoluble deposit and impure particles by filtering through a 0.22 μm membrane syringe filter (Rankem, India). The carbon nanodot-containing supernatant was termed qCD. Further, to investigate the effect of surface fabrication on the metal sensing ability of qCD, it was fabricated using polyethylene glycol. PEG-passivated CNDs were prepared by a similar scheme but with the addition of PEG and were referred to as qCD-Pg.

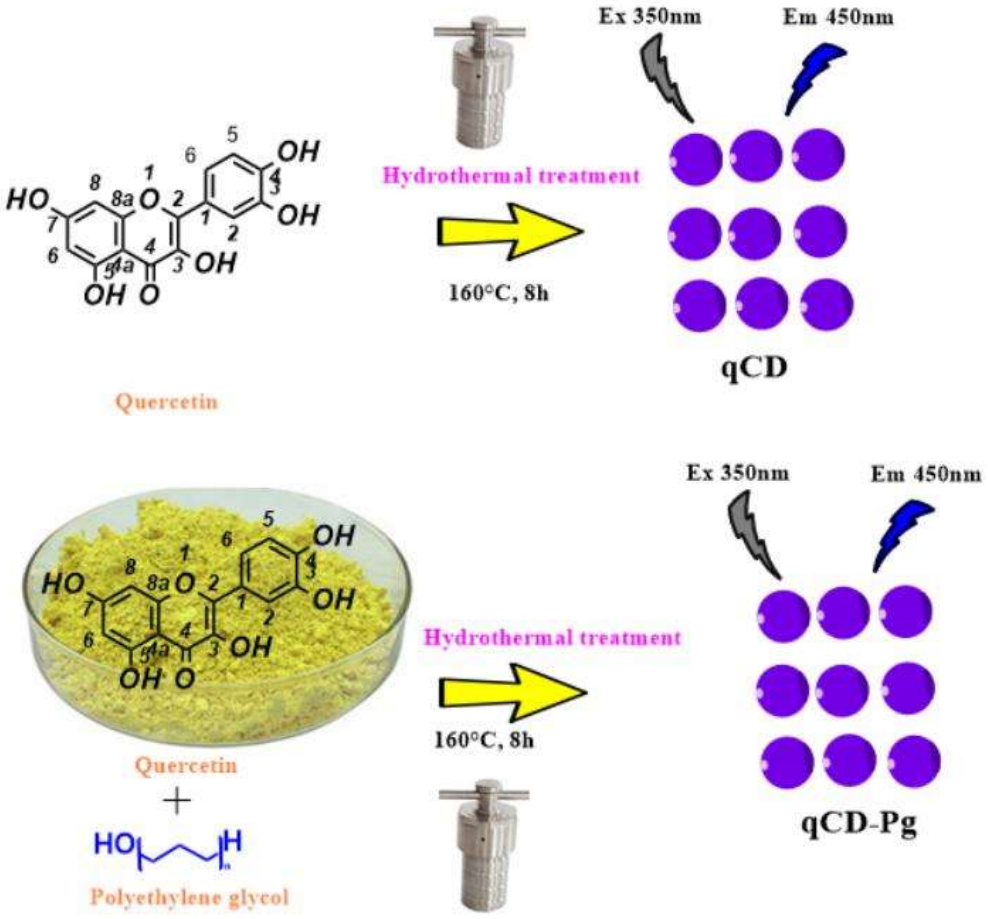


**Scheme 7.1** Schematic of the synthetic process for quercetin-based CNDs via a one-step hydrothermal treatment.

### 7.2.3 Andrographolide isolation and characterization from AP leaves

The collected samples were dried and then powdered using a grinder (Phillips). The powdered AP leaves (1000 g) were initially extracted with methanol using soxhlet apparatus. The obtained crude extracts in solution form were evaporated under a vacuum and dried. The dried sample (159.75 g) was dissolved in small amounts of water and then was further partitioned with organic solvents to yield hexane (9.27 g) and ethyl acetate

(65.75 g), and n-butanol (15.02 g) fractions. The ethyl acetate fraction consisted of a greenish crystalline mass dissolved in HPLC grade methanol with a hot charcoal solution. The mixture was filtered out right away, and the filtrate was left to crystallize. The resulting crystalline powder was studied by UV spectroscopy, FT-IR, XRD, melting point determination, $^{1}$H NMR, and $^{13}$C NMR.

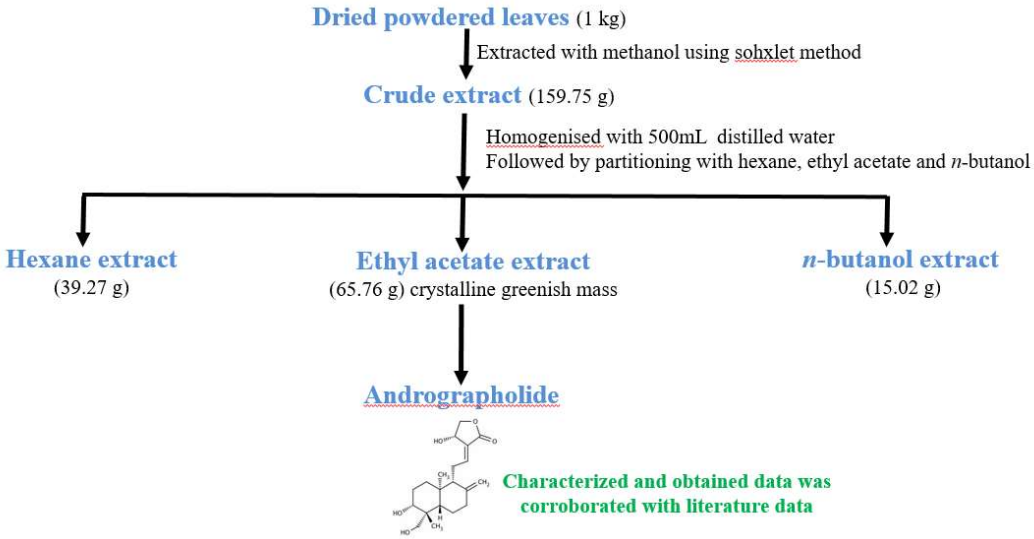


**Scheme 7.2** Isolation of Andrographolide.

### 7.2.4 Loading of andrographolide (Ad) and the release behavior of qCD-Pg-Ad

Following earlier literature, the loading and release behaviour of the qCD-Pg-Ad complex was investigated [Shi *et al.,* 2021, Zhou *et al.,* 2022]. To load Ad onto CNDs, the CNDs were blended with Ad solution (50 mg mL$^{-1}$) in ethanol and shaken for 24 hours at room temperature under dark conditions. To remove the unloaded drug, the solution was dialyzed for 12 h against one-liter ultrapure water: ethanol mixture (9.5:0.5). For later usage, the dialyzed CNDs-Ad conjugate solution was kept at 4° C. The absorbance was measured at 230 nm to acquire the free drug's standard calibration curve, which was used

to compute the drug loading efficiency (DLE). The DLE was computed in the following manner:

$$\% \text{ DLE} = \frac{\text{Amount of Ad in qCD–Pg–Ad}}{\text{Amount of Ad taken}} \times 100 \quad (7.1)$$

The *in-vitro* drug release behavior experiments were performed: After dissolving the qCD-Pg-Ad complex in 3 mL of pH 7.4 or 5.4 PBS, the solution was sealed in a dialysis bag with a 12 kDa molecular weight cutoff (Himedia, India). Due to the solubility issues of poorly water soluble andrographolide, we have used 2% tween 80 with PBS as release media to maintain the sink condition. This dialysis bag was placed in 27 mL PBS solution and shaken at room temperature at 100 rpm (Remi, India). The qCD-Pg-Ad complex was dissolved in 3 mL of pH 7.4 or 5.4 PBS solution, and the solution was sealed in a dialysis bag with a molecular cutoff weight of 12 kDa (Himedia, India), placed in PBS solution (27 mL), and shaken at 100 rpm at room temperature (Remi, India). UV-visible (UV-Vis) analysis was carried out at selected time points (0.5h, 1h, 2h, 4h, 6h, 8h, 12h, 24h, 48h, 72h), withdrawing 3 mL of buffer solution outside the dialysis bag, supplemented with fresh PBS solution (3 mL). The release of Ad was measured at 230 nm using a standard calibration curve (y =0.016x-0.0395, $R^2$= 0.9982) for andrographolide at room temperature.

### 7.2.5 Characterization, optical properties and stability studies

The absorption behavior of the synthesized CNDs was investigated using a UV–vis double beam spectrophotometer (Cary 60 UV vis, USA). The fluorescence attributes of CNDs were studied by employing a Fluorolog-Horiba fluorescence spectrophotometer. Fourier transform infrared spectrometer (Shimadzu FTIR-8400S, Japan) was used to

examine the surface functional groups in 4000-400 $cm^{-1}$. HR-TEM (Tecnai G2 20 TWIN, USA) analysis of the CNDs was conducted to study their morphology. After calculating the size of 50 particles with ImageJ software, the average particle size was computed. Elemental analysis was performed using Energy dispersive X-ray spectroscopy (EDAX Inc.'s TEAM EDS SYSTEM), and selected area diffraction (SAED) patterns were obtained using Octane Plus SDD Detector. K-Alpha, Thermo Fisher Scientific, was utilized to record X-ray photoelectron spectroscopy. Rigaku Miniflex 600 Desktop X-Ray Diffraction System was utilized to obtain X-ray diffraction (XRD) patterns of CNDs. Apart from this, colloidal dispersion stability (by measuring zeta potential), photostability (UV illumination with an excitation wavelength of 350 nm), and thermal stability (using TGA-50 thermogravimetric analyzer) of CNDs were also investigated.

## 7.3 Applications of CNDs

### 7.3.1 Metal sensing

The sensing ability of relevant metal ions by qCD and qCD-Pg was studied as per earlier reported studies with slight modifications [Rahimi *et al.,* 2021]. The sensing selectivity of qCD towards various metal cations such as $Mg^{2+}$, $Hg^{2+}$, $Fe^{3+}$, $Ba^{2+}$, $Cu^{2+}$, $Ca^{2+}$, $K^{+}$, $Na^{+}$, $NH_4^{+}$, $As^{3+}$, $Ag^{+}$, $Bi^{3+}$, and $Pb^{2+}$ was analyzed by adding 2 mL of qCD solution (250µg/mL) to 2 mL of aqueous metal solutions, with the final concentration of 200µM of each metal ion. After incubating for 5 min, the fluorescence intensity was measured using 3nm slit width and 350 nm excitation wavelength. Metallic ion $As^{3+}$ was able to enhance the fluorescence of qCD significantly. Further to study the passivation effect on the $As^{3+}$ sensing ability of qCD, Polyethylene glycol (Pg)-passivated qCD termed as qCD-Pg (250µg/mL) were analyzed for their sensing selectivity using different

metal ions mentioned above. To study the sensitivity of qCD and qCD-Pg towards $As^{3+}$ and $Fe^{3+}$ respectively, fluorescence titrations were carried out using different concentrations of an aqueous metal cation and measuring the fluorescent intensities at the same excitation wavelength. The Stern-Volmer equation was used to analyze the quenching efficiency of metallic ions. The following equation was used for computing the limit of detection (LOD) of CNDs on a selected metal ion:

$LOD=3\sigma/s$

Where s is the slope of the linear line and σ is the standard deviation of $F^0/F$ values.

### 7.3.2 Cytotoxicity against K-562 leukemia cell lines

The cell lines were cultured in a medium that contained 10% foetal bovine serum and two mM L-glutamine. For this screening experiment, a hundred (100) µL of cell suspension containing 5000 cells per well were inoculated onto a 96-well microtiter. To evaluate the cytotoxicity potential of the CNDs and its conjugates, K-562 Leukemia cancer cells and normal Vero cell lines were treated with different concentrations (10 µg/ml, 20 µg/ml, 40 µg/ml, and 80 µg/ml) of qCD, qCD-Pg, qCD-Pg-Ad, Ad and Adriamycin (as positive control). The cytotoxicity of either non-cancerous or cancerous cells was investigated by employing sulforhodamine B colorimetric assay, and the $IC_{50}$ (in µg /mL) was computed using previously described methods [Meher *et al.,* 2021, Kholiya *et al.,* 2020]. The images of samples tested (highest drug concentration used) were captured using Ti-S Inverted Research Microscope- Nikon with a magnification of ×20, with Eclipse Image processing software NIS-Elements.

### 7.3.3 Viability studies using MDR bacterial strains

The antibacterial activities of qCD, qCD-Pg and qCD-Pg-Ad were evaluated using the previously reported paper disk diffusion method with slight modifications [Souri *et al.,* 2021]. The test clinically isolated MDR bacteriae *Enterobacter cloacae* (G-), *Escherichia coli* (G-), *Klebsiella pneumonia* (G-), *Enterococcus faecium* (G+), and *Staphylococcus aureus* (G+) were grown at 37 °C on nutrient agar for 18 h. Then bacterial suspensions were prepared by inoculating them into a sterilized medium. A 100µL of bacterial suspension containing $10^8$ CFU/mL with $OD_{600}$ was coated on MHA medium plates. Then, paper discs were placed on a pre-sterilized filter, and 20µL of 5.00 mg/mL, 9.00 mg/mL, and 40.00 mg/mL of qCD, qCD-Pg, and qCD-Pg-Ad, respectively, were pipetted onto paper discs. After incubating at 37 °C for 24 h, inhibition zones were computed and compared. To obtain statistically significant data, at least three independent experiments were performed.

### 7.3.4 Free radical scavenging activities of CNDs

Free radicals scavenging potential of qCD, qCD-Pg, and qCD-Pg-Ad was evaluated according to the previously reported method with slight modifications [Alamu *et al.,* 2021]. A 2 mL of DPPH methanolic solution (5.9 mg/100 mL methanol) was added to different concentrations (0-250 µg/ml) of samples, amounting to 1 mL, and then incubated in the dark at room temperature for 30 minutes. The absorbance was read at 515 nm, and percent radical scavenging activity was calculated.

### 7.3.5 Statistical analysis

At least three independent experiments were performed to obtain significant data and expressed as n ± SD. The statistical analysis was carried out using Student's t-test in

Graph Pad Prism Version 5.0. $P < 0.05$ was used as the criterion for statistical significance.

## 7.4 Results and Discussion

### 7.4.2 Formation of CNDs

CNDs were synthesized employing quercetin (termed qCD) and another by surface passivating with polyethylene glycol (termed qCD-Pg) via a simple one-step hydrothermal treatment at 160 °C for a period of 8 h as depicted in Scheme **7.1**. As shown in Scheme **7.2**, the isolated Andrographolide was characterized using UV-Vis spectroscopy, FT-IR, $^{1}$H NMR, and $^{13}$C NMR. The obtained data were corroborated with the reported literature data [Rajani *et al.,* 2000, Fujita *et al.,* 1984]. Isolated Ad had a melting point of 234.9±0.5$^{o}$C.

### 7.4.3 Characterization of CNDs

HR-TEM was performed to study the size and nature of the phase of CNDs. As shown in Figure **7.1 a** and **7.1 b**, the average diameter for qCD and qCD-Pg was determined to be 1.3-1.9 nm and 3.0-3.8 nm, respectively, while qCD-Pg-Ad was 4.2-4.9 nm (Figure **7.1 c**). CNDs were spherical and evenly distributed. Additionally, SAED patterns (Figure **7.1 d**, **7.1 e**, **7.1 f**) of CNDs revealed dispersed rings, confirming their amorphous phase. The amorphous form of CNDs indicates that they were appropriately fabricated. Elemental composition was analyzed for qCD and qCD-Pg by Energy dispersive X-ray spectroscopy (EDS) via HR-TEM. As shown in Figure **7.1 g** and **7.1 h**,

a significant amount of oxygen, carbon, and nitrogen was observed, according to the low positive zeta potential value of qCD and qCD-Pg.

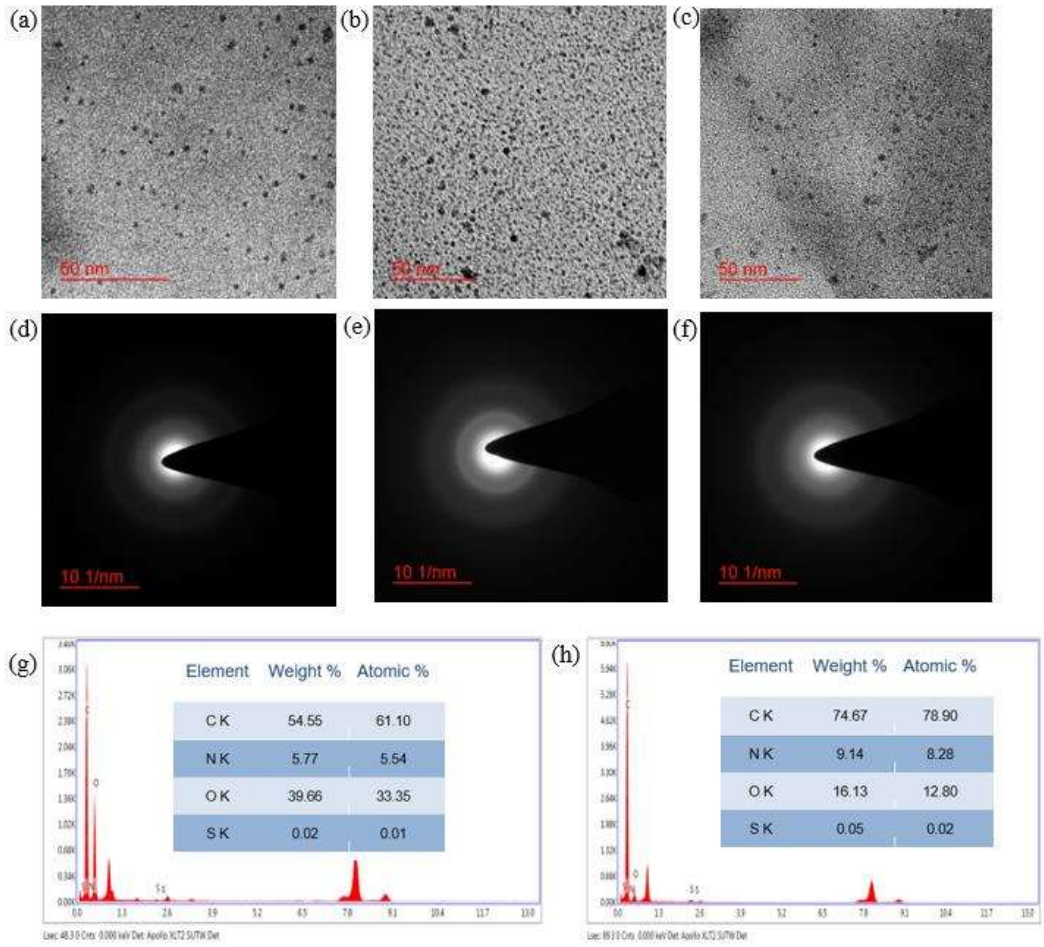


**Figure 7.1**. Surface morphology, Selected area electron diffraction pattern and Energy-dispersive x-ray spectroscopy of CNDs and its conjugates [a] HR-TEM image at a 50 nm resolution showing uniform dispersity [b] HR-TEM image at a 50 nm resolution showing uniform dispersity [c] HRTEM image at a 50 nm resolution showing uniform dispersity [d] Selected area electron diffraction pattern of qCD [e] and Selected area electron diffraction pattern of qCD-Pg [f] Selected area electron diffraction pattern of qCD-Pg-Ad [g] Energy-dispersive x-ray spectroscopy spectra of qCD with inset data showing the elements with their corresponding percentage [h] Energy-

dispersive x-ray spectroscopy spectra of qCD-Pg with inset data showing the elements with their corresponding percentage.

### 7.4.4 Drug release studies

The fluorescence spectroscopic study verified the effective conjugation of Ad on CNDs. The blue-shifting observed in qCD-Pg-Ad at 435 nm compared to qCD-Pg at 450 nm likely demonstrates the successful conjugation of the Ad (Figure **7.2 a**). At pH 7.4 and 5.4, the efficacy of Ad release was studied and the cumulative drug release paradigms were displayed using UV-vis spectroscopic analysis. As shown in Figure **7.2 b**, over 72 hours, the Ad release rate for the conjugates was significantly faster in acidic conditions (pH 5.4) than in pH 7.4 (physiological condition).

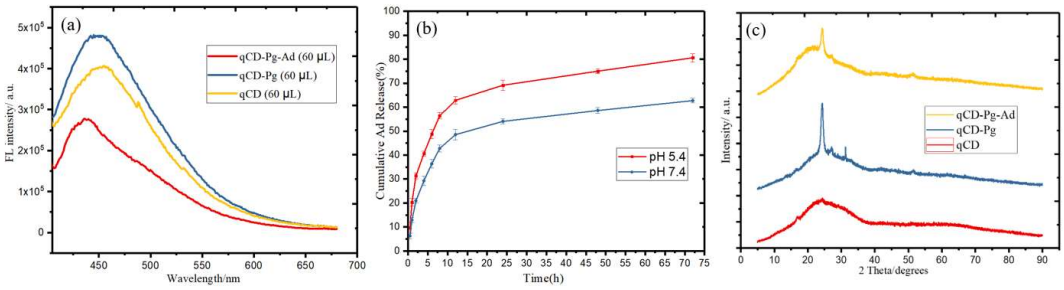


**Figure 7.2** [a] FL spectra of qCD, qCD-Pg, qCD-Pg-Ad [b] The cumulative Ad release paradigms of qCD-Pg-Ad at pH 7.4 and 5.4. Each data point represents the average of triplicate measurements, and the error bars represent the standard deviation [c] X-ray diffraction spectrum of qCD, qCD-Pg, qCD-Pg-Ad, and Ad.

Andrographolide demonstrated a biphasic release pattern with an initial burst release up to 8 h and a sustained release pattern up to 72h. It could be possible that the initial phase of drug leaching may be due to weak physical adsorption of the drug on CNDs' surfaces; however, stronger interactions between CNDs and the drug could have led to a sustained

release pattern [Nigam *et al.,* 2014, Shamsipour *et al.,* 2019]. Also, the biphasic pattern could be possibly due to homomolecular interactions between drug-drug in the outer layer, leading to the fast release of the drug. In contrast, heteromolecular interaction between CNDs-drug on the surface could be responsible for the sustained release of the drug. The initial burst release may assist in killing cancerous cells in a short period, and sustained drug release would maintain the required therapeutic dose [Saneja et al., 2017]. As demonstrated in Figure **7.2 c**, the XRD pattern of qCD has a poor crystallinity compared to qCD-Pg and qCD-Pg-Ad. The prepared carbon dots' XRD patterns show a strong peak at 2θ= 24.3° (d = 0.36 nm), and a small peak at 2 θ = 27.06º (d = 0.33 nm) corresponding to the diffractions at amorphous carbon phase and graphitic carbon, respectively [Hu *et al.,* 2018, Zhang *et al.,* 2015].

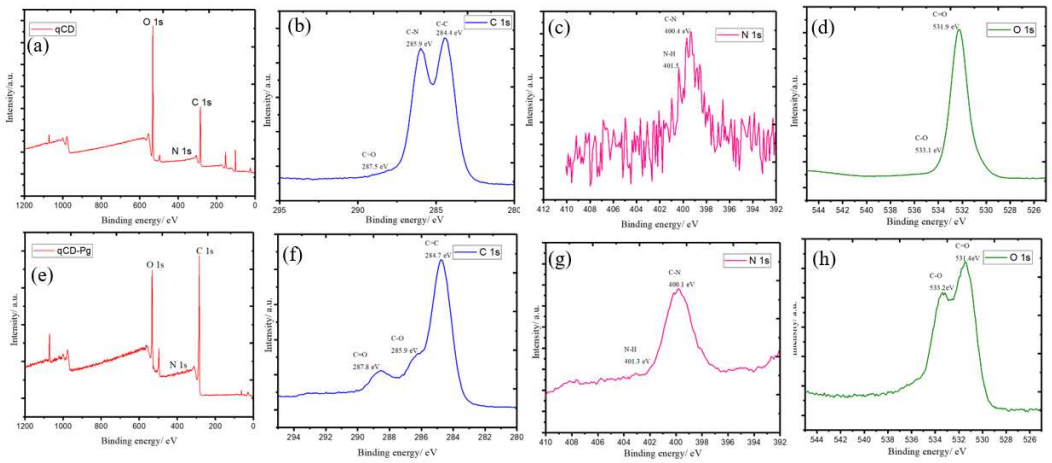


**Figure 7.3**. [a] XPS survey spectra of the qCD [b] XPS high-resolution survey scan of C 1s, [c] N 1s and [d] O 1s region of qCD [e] XPS survey spectra of the qCD-Pg [f] XPS high-resolution survey scan of C 1s, [g] N 1s and [h] O 1s region of qCD-Pg. [i] Thermogravimetric analysis spectrum of CNDs [j] Zeta potentials of qCD, qCD-Pg, qCD-Pg-Ad.

Figure **7.3 a** and **7.3 e** shows the XPS spectra of qCD and qCD-Pg respectively, which revealed three distinct peaks corresponding to C 1s, N 1s, and O 1s at 285.08, 400.54, and 532.08 eV, respectively, which confirmed the availability of C, N, and O containing functional groups on the surface of CNDs. In the C 1s spectrum of qCD, peaks at 285.9 and 284.4 eV could be attributed to C-O/C-S/C-N bonds and C-C bonds, respectively (Figure **7.3 b**). Figure **7.3 c** shows N 1s spectra of qCD, which revealed two peaks at 400.4 eV (C-N-C) and 401.5 eV (quaternary ammonium groups). In the O 1s spectrum of qCD (Figure **7.3 d**), peaks at 531.9 and 533.1 eV could correspond to C=O and COH/COC, respectively [Saraswat *et al.,* 2022, Liu *et al.,* 2022]. Similarly, in the C 1s spectrum of qCD-Pg, peaks at 285.9 and 284.7 eV could be attributed to C-O/C-S/C-N bonds and C-C bonds, respectively (Figure **7.3 f**). The C=O bond was attributed to the peak at 287.8 eV. Figure **7.3 g** shows N 1s spectra of qCD-Pg, revealing two peaks at 400.1 eV (C-N-C) and 401.3 eV (quaternary ammonium groups). In the O 1s spectrum of qCD (Figure **7.3 h**), peaks at 531.9 and 533.1 eV could correspond to C=O and COH/COC, respectively [Saraswat *et al.,* 2022, Liu *et al.,* 2022]. The XPS and FTIR results confirmed the presence of various functional groups in different forms, which may be responsible for variations in their Physico-chemical and biological profiles.

### 7.4.5 Optical properties of CNDs

Under a UV lamp, the as-prepared qCD, qCD-Pg, emitted a strong blue-green fluorescence and to confirm the effective conjugation of andrographolide on CNDs, UV-Vis and fluorescence spectroscopies were used to analyze the CNDs conjugates.

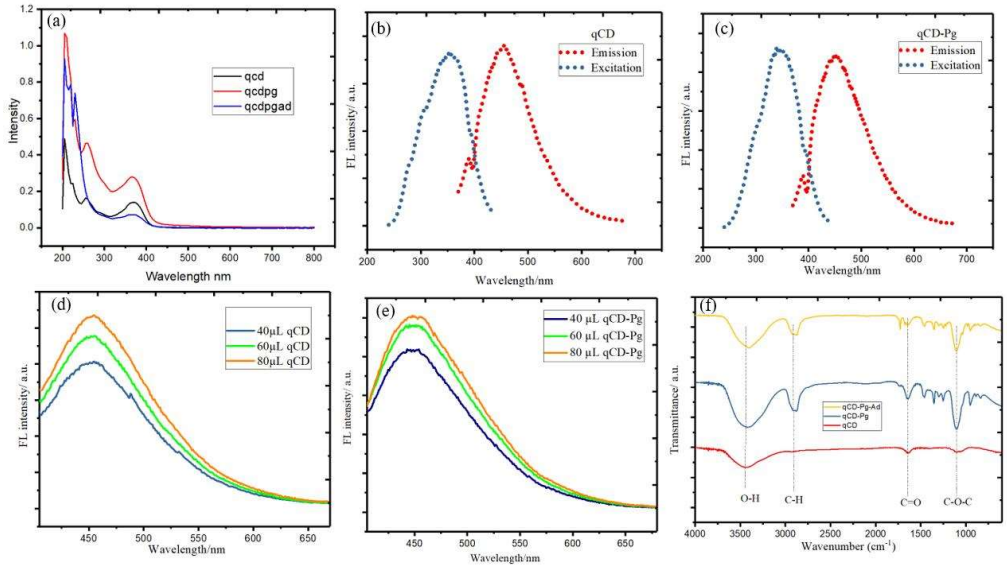


**Figure 7.4.** [a] UV-visible absorption spectra [b] FL spectra of qCD [c] FL spectra of qCD-Pg [d] concentration-dependent FL spectra of qCD at an excitation wavelength of 355 nm [e] concentration-dependent FL spectra of qCD-Pg at an excitation wavelength of 350 nm [f] FT-IR spectrum.

Figure **7.4 a** exhibits the UV-vis absorption spectra of CNDs which revealed peaks at 255 and 367 nm, attributed to π to π* and n to π* transitions, respectively. Absorption peaks in the 300-400 nm range may correspond to transitions related to C=N and C=O groups. When excited at 350 nm, qCD and qCD-Pg fluorescence were recorded at 400-550 nm, with the maximum at 450 nm, as shown in Figure **7.4 b** and **7.4 c**. Figures **7.4 d** and **7.4 e** show the concentration-dependent fluorescence spectra of qCD and qCD-Pg.

The typical andrographolide absorption band of 230 nm revealed the existence of andrographolide in the conjugates of qCD-Pg-Ad (Figure **7.4 a**). Due to the absorption of andrographolide molecules, an absorption peak in the UV-vis spectrum of the qCD-Pg-Ad spectrum was centred at around 230 nm following loading with andrographolide. UV-vis spectroscopy was employed to calculate the concentration of loaded andrographolide

in carbon nanodots conjugate. Ad's strong excitation was identified around 230 nm; hence it was measured quantitatively using a calibration curve. The average DLE percent of the qCD-Pg-Ad was 29.3± 0.4 percent based on three distinct batches.

FT-IR analysis was used to assess the presence of surface functionalities on CNDs, and the findings are displayed in Figure **7.4 f**. The CNDs' OH/NH and carbonyl stretching were attributed to broad peaks at around 3936 and 1645 $cm^{-1}$, respectively. Peaks between 1215 and 985 $cm^{-1}$ could be related to oxygen-containing functional groups' C-O stretching vibrations. Solubility and stability are provided by the polar functional groups that occur on the surface of CNDs. In addition to these peaks, qCD-Pg-Ad had two sharp peaks at 1723 and 1672 $cm^{-1}$, implying that Androgapholide could interact with qCD-Pg via electrostatic interactions [ Hailing *et al.,* 2020, Kong *et al.,* 2018, Yuan *et al.,* 2017].

### 7.4.6 Stability studies of CNDs

As shown in Figure **7.5 a**, quercetin's zeta potential (ZP) was -17.55 mV; however, the ZP of quercetin-derived CNDs was -18.10 mV. This is owing to the loss of some of the quercetin's functional groups during the fabrication of CNDs. The ZP of qCD upon surface passivation with PEG (10.45 mV) was drastically changed and found to be -7.1 mV. The ZP analysis was further utilized to confirm the binding of qCD-Pg to Ad. qCD-Pg exhibited a negative charge (-7.1 mV), whereas upon conjugation with Ad (-8.37 mV), the ZP of resulted qCD-Pg-Ad complex exhibited ZP of -16.6 mV. Negatively charged plasma membranes of living cells and high electrostatic affinity towards positively charged nanoparticles facilitates tumor entry of nanoparticles via the Enhanced permeability and retention (EPR) effect. The increasing size and ZP of the CNDs after

passivation (Figure **7.3**) confirms efficient passivation with PEG and further conjugation with Ad.

The TGA spectrum shown in Figure **7.5 b** indicates the thermal behaviour of CNDs in terms of weight loss at different temperatures. A three-step degradation pattern was observed in the thermograms of qCD and qCD-Pg, indicating their thermal stability up to 900°C. The curve leveled off after 999 °C, and a small quantity of CNDs remained as burnt carbon. Earlier studies [Mewada *et al.,* 2013, Mehta *et al.,* 2014] have made similar observations. The photostability studies of qCD and qCD-Pg were studied by exposing them to UV light for 120 min and then determining the changes in absorbance and intensity at different time points. As shown in Figure **7.5 c**, no major photobleaching of CNDs was observed after continuous UV exposure, and fluorescence remained unaltered.

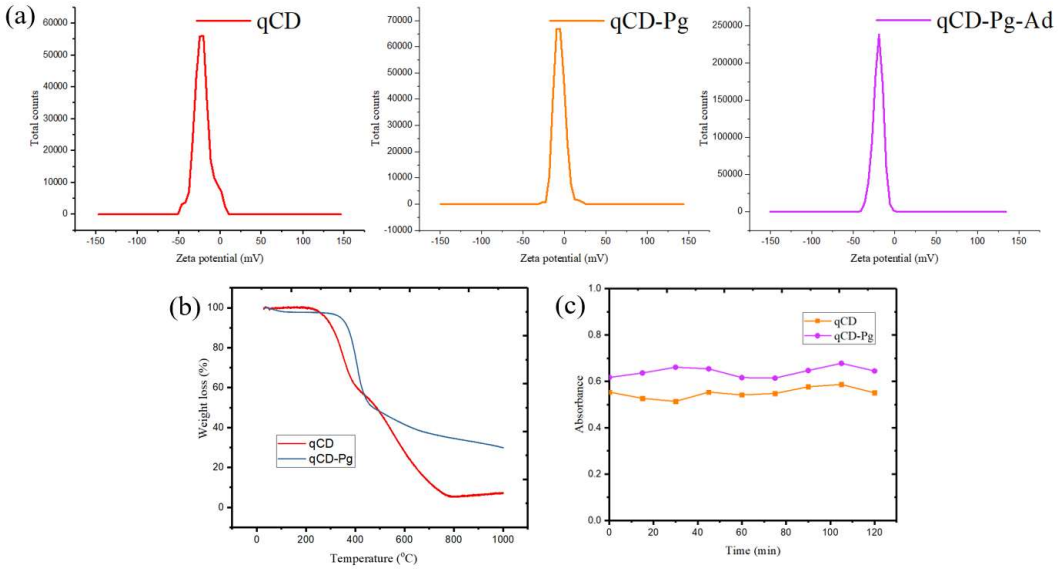


**Figure 7.5**. Stability studies of CNDs [a] Zeta potentials of qCD, qCD-Pg, qCD-Pg-Ad [b] Thermogravimetric analysis spectrum of CNDs [c] Photostability study of CNDs.

### 7.4.7 Applications of CNDs

*7.4.7.1 Metal sensing*

Selectivity is a critical criterion for evaluating CNDs' performance. Thus, we investigated the differences in fluorescence emission intensity by adding various biologically and environmentally relevant metal ions to the qCD at a concentration of 200 µM, including $Mg^{2+}$, $Hg^{2+}$, $Fe^{3+}$, $Ba^{2+}$, $Cu^{2+}$, $Ca^{2+}$, $K^{+}$, $Na^{+}$, $NH^{4+}$, $As^{3+}$, $Ag^{+}$, $Bi^{3+}$, and $Pb^{2+}$, and obtaining the corresponding fluorescence emission spectra.

$As^{3+}$ had the most considerable propensity to enhance the fluorescence intensity of qCD among the metal ions, whereas $Fe^{3+}$ had the highest tendency for quenching the fluorescence intensity of qCD. Furthermore, to investigate the impact of surface fabrication of polyethylene glycol (PEG4000) on the ability of qCD to sense metals, qCD-Pg were tested for metal sensing, and it was discovered that qCD-Pg was unable to selectively sense $As^{3+}$ due to a change in the nature of surface functional groups, but retained the ability to sense $Fe^{3+}$.

As a result, a sensitivity titration was carried out at various $As^{3+}$ concentrations ranging from 0 to 200 µM. The emission of the qCD at 450 nm progressively increased as the concentration of $As^{3+}$ increased, as shown in Figure **7.6 a**; this demonstrates that the current sensing system is sensitive to $As^{3+}$. The relation between $F_0/F$ and $As^{3+}$ concentration is presented in the inset. A correlation value ($R^2$) of 0.995 found a good linear relationship between the linear ranges at 40–100 µM, as illustrated in Figure **7.6 b**. The LOD was discovered to be 0.763µM.

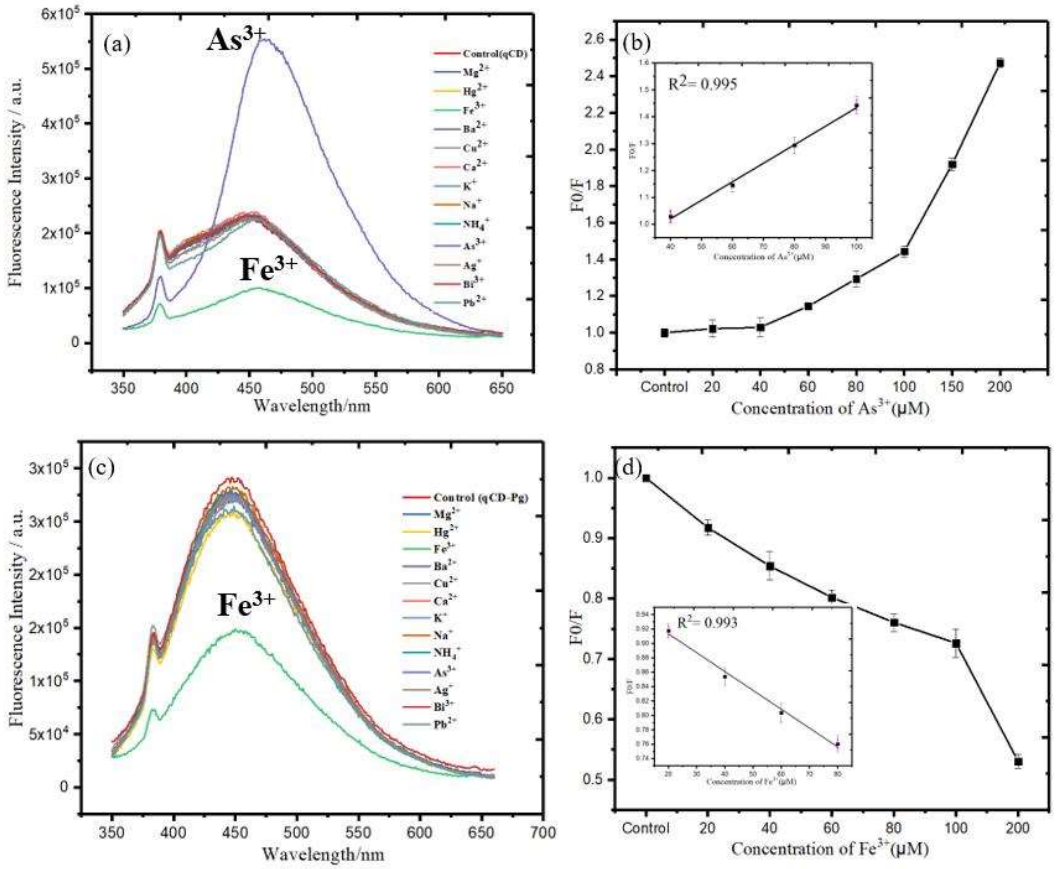


**Figure 7.6**. Sensing of Metal ions using CNDs [a] Fluorescence responses of qCD toward various metal ions. The control represents the fluorescence response of the CNDs without any ion. [b] Fluorescence intensity of qCD versus concentration of $As^{3+}$ from 0 to 200 μM (inset image showing linearity, with $F_0$ and F being the fluorescence intensities in the absence and presence of $As^{3+}$, respectively.) [c] Fluorescence responses of qCD-Pg toward various metal ions. The control represents the fluorescence response of the CNDs without any ion. [d] Fluorescence intensity of qCD-Pg versus concentration of $Fe^{3+}$ from 0 to 200 μM (inset image showing linearity, with $F_0$ and F being the fluorescence intensities in the absence and presence of $Fe^{3+}$, respectively.)

A sensitivity titration was also carried out at various $Fe^{3+}$ concentrations ranging from 0 to 200 μM. The emission of the qCD-Pg at 450 nm steadily declined as the concentration of $Fe^{3+}$ increased, as shown in Figure **7.6 c**; this demonstrates that the current sensing

system is susceptible to $Fe^{3+}$. The relationship between $F_0/F$ and $Fe^{3+}$ concentration is shown in the inset. Figure **7.6 d** shows a good linear relationship between the linear ranges at 20–80 μM, with a correlation coefficient ($R^2$) of 0.993. The LOD was discovered to be 0.728μM.

In the case of qCD, the addition of $As^{3+}$ results in a significant increase in fluorescence compared to the control. The aggregation process, which subsequently produced the aggregation-induced enhanced emission (AIEE) mechanism activity of qCD, is thought to be caused by the complex formation and intramolecular and extramolecular interactions. AIEE active probes are mildly emissive in the aggregate state, but they become substantially emissive in the aggregate state. Non-radiative decay routes are hindered in the aggregate state due to restricted intramolecular rotation [Tian *et al.,* 2017, Shyamal *et al.,* 2016, Chen *et al.,* 2013]. As a result, increased emission triggered by aggregation, where analytes aggregate through electrostatic, metal coordination, and hydrogen bonding, can be employed as a sensing probe. This behavior also helps to overcome flaws in traditional fluorophores, such as aggregation-triggered quenching, fluorescence bleaching, and asymmetric emission [Tian *et al.,* 2017, Shyamal *et al.,* 2016, Chen *et al.,* 2013]. Multiple intermolecular contacts between qCD and arsenic ions caused aggregation in the presence of $As^{3+}$, blocking non-radiative decay pathways and populating the radiative decay pathways. The presence of several functional groups on the surface of qCD, such as $OH^{2+}$, OH, and O, may explain its adsorptive behavior, and arsenic ion species can bind to qCD via intramolecular or extra-molecular interactions or adsorption [Kumar *et al.,* 2017].

For $Fe^{3+}$ sensing, ground-state complex formation, collision quenching, excited-state reaction, molecule rearrangement, and energy transfer are intermolecular interactions responsible for fluorescence quenching [Zhao *et al.,* 2019, Qi *et al.,* 2019]. Static quenching and dynamic quenching are two types of quenching mechanisms. The electron transfers from excited qCD-Pg to half-filled 3d orbitals of $Fe^{3+}$ caused strong non-radiative electron/hole recombination, resulting in aggregation-induced emission quenching [Zhao *et al.,* 2019, Qi *et al.,* 2019]. indicating that $Fe^{3+}$ ions bind to the functional groups on the surface of qCD-Pg to form $Fe^{3+}$ chelates. As a result of the coordination of $Fe^{3+}$ on the surface of qCD-Pg with nitrogen-bearing groups, carboxyl and hydroxyl, the radiation transition is destroyed, and fluorescence quenching occurs [Khan *et al.,* 2019, Wang *et al.,* 2017].

*7.4.7.2 Cytotoxicity against K-562 leukemia cell lines*

The cytotoxicity of qCD, qCD-Pg, and qCD-Pg-Ad was investigated *in-vitro* against K-562 (leukemia cell line) and Vero cells (Normal kidney cells) using the sulforhodamine–B (SRB) assay. The percent control growth is computed by comparing test growth (treated) to control growth (untreated), with untreated percent growth assumed to be 100%. The results were expressed as $IC_{50}$ (inhibition 50%) values. The anticancer screening findings (Figure **7.7**) demonstrated that qCD-Pg-Ad could be a potent anticancer drug with notable $IC_{50}$ values of 43 µg/mL, indicating that it is likely to be used to treat leukemia. When free Ad was loaded onto CNDs, the $IC_{50}$ value (60.2 µg/mL) was enhanced. Interestingly, no substantial cytotoxicity was seen in the normal kidney (Vero) cell line up to 80 µg/mL when observed in brightfield microscope, indicating that these CNDs have only cancerous cell targeting potential. Cytotoxic effect

of CNDs on the % cell growth of Vero and K-562 leukemia cell lines is shown in Table **7.1.**

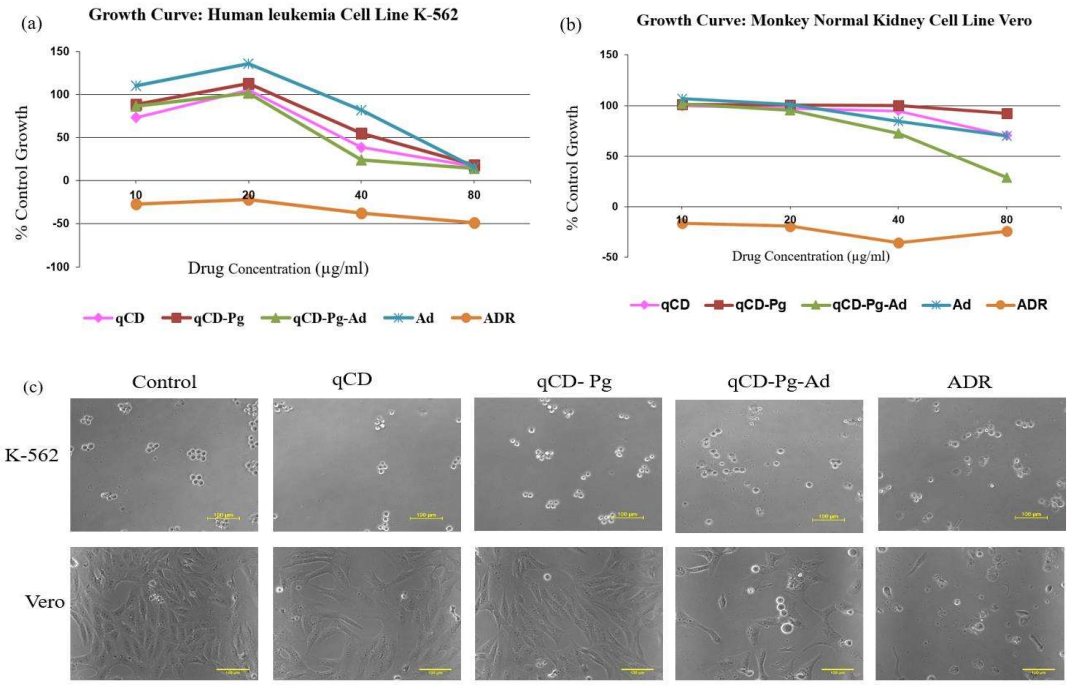


**Figure 7.7**. [a] Cytotoxic effect of CNDs on the % cell growth of K-562 leukemia cancer cell lines. [b] Cytotoxic effect of CNDs on the % cell growth of normal vero cell lines. We present data as the mean percent cell growth in the presence of 4 different concentrations of CNDs in comparison with negative cell control. We tested all concentrations in triplicates and repeated the experiment three times. ADR = Adriamycin (taken as a positive control compound). [c] Bright field microscopy which shows cell morphology of cell cultures incubated at 48 h. Scale bar of 100 µm is shown at lower right of each panel.

*7.4.7.3 Viability studies using MDR bacterial strains*

The antibacterial activity of qCD, qCD-Pg and qCD-Pg-Ad was examined against different clinically isolated MDR bacterial strains. i.e., *Escherichia coli* (G-), *Klebsiella*

*pneumonia* (G-), *Enterobacter cloacae* (G-), *Enterococcus faecium* (G+), and *Staphylococcus aureus* (G+) using disk diffusion method with slight modifications. As provided in Table 7.**2** and Figure **7.8**, it revealed significant zones of growth inhibition against these MDR strains cells around the discs supplemented with 20 µL of qCD (5mg/mL), qCD-Pg (14mg/mL), and qCD-Pg-Ad (40mg/mL). These findings suggested that qCD-Pg-Ad is more effective than Ad at preventing microbial growth.

Nanoparticles such as these CNDs can rupture the membrane and create free radicals, which ultimately lead to their death [Hajipour *et al.,* 2012]. This is owing to the small size of bacterial cells and the high surface-to-volume ratio of nanoparticles. This research work projects qCD-Pg-Ad as a potential antibacterial therapeutic agent; however, in-depth *in-vivo* studies would help understand its pharmacokinetics and pharmacodynamics.

*7.4.7.4 Free radical scavenging activity*

Dose-dependent free radicals scavenging potential of qCD, qCD-Pg, qCD-Pg-Ad was determined using DPPH assay. It was observed that with an increase in the concentrations of qCD, qCD-Pg, and qCD-Pg-Ad, DPPH absorbance was decreased, as shown in Figure **7.9**. DPPH was converted into a stable DPPH-H complex after accepting a hydrogen radical, which made the solution pale yellow from deep violet. The leftover DPPH was determined by comparing absorbance to blank at 515 nm. It can be inferred from the obtained results that the free radical scavenging potential of qCD was improved after surface passivation with PEG and subsequent conjugation with Ad.

**Table 7.1**. Cytotoxic effect of CNDs on the % cell growth of Vero and K-562 leukemia cell lines.

| **Sample** | **Drug concentration (µg/mL) $IC_{50}$** | |
|---|---|---|
| | **Vero Cell lines** | **K-562 cell lines** |
| Qcd | >80 | 45.5 |
| qCD-Pg | >80 | 52.6 |
| qCD-Pg-Ad | 60.6 | 42.8 |
| Ad | >80 | 60.2 |
| ADR | <10 | <10 |

**Table 7.2**. Zones of inhibition against different bacterial strains.

| **Bacterial strain** | **Average radial diameter growth inhibition zone (in mm)** | | | | | |
|---|---|---|---|---|---|---|
| | Qcd | qCD-Pg | qCD-Pg-Ad | Ad | Doxicyclin positive control | DMSO |
| *E. cloacae* | 12±0.4 | 14±0.5 | 15±0.3 | 12±0.5 | 16±0.9 | - |
| *E. coli* | 7±0.2 | 8±0.8 | 16±0.4 | 7±0.5 | 19±0.7 | - |
| *K. pneumonia* | - | - | - | - | 16±0.2 | - |
| *S. aureus* | - | - | - | - | 21±0.3 | - |
| *E. faecium* | 6±0.8 | 8±0.2 | 14±0.4 | 7±0.6 | 15±0.1 | - |

**(Data was represented as mean± SD)**

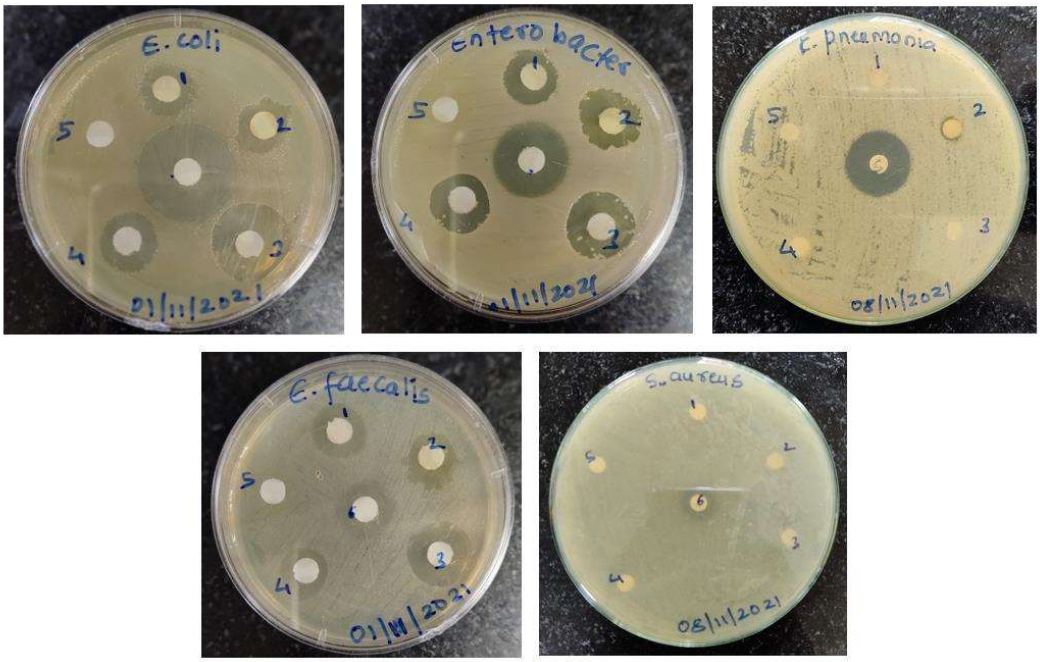


**Figure 7.8.** Anti-bacterial assay against clinically isolated multi-drug resistant strains with doxyclycline (positive control) and water (negative control). 1- qCD, 2-qCD-Pg, 3-qCD-Pg-Ad, 4- Ad, 5- DMSO, 6- Doxicycline as positive control.

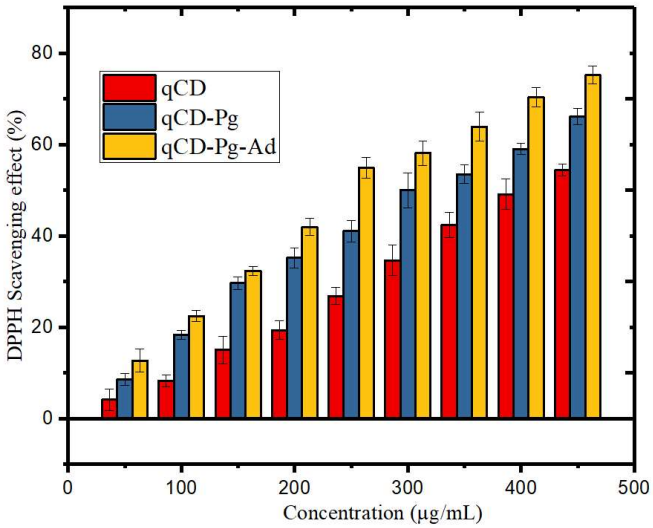


**Figure 7.9.** % DPPH scavenging activity for various concentrations of qCD, qCD-Pg, qCD-Pg-Ad.

## 7.5 Conclusion

In this objective, we fabricated quercetin-based CNDs using the hydrothermal method and characterised by XPS, XRD, HR-TEM, FT-IR, TGA, and zeta potential. The generated CNDs exhibited several valuable characteristics, including strong photostability, a nano-carrier for the model drug andrographolide against leukemia cells, a nano-probe for sensing $As^{3+}$ and $Fe^{3+}$, and antibacterial activity against MDR bacteria, and free radical scavenging capability. Overall, our findings showed that quercetin-based CNDs are good contenders for various biological and environmental applications.